Level Set Topology Optimization of Load Carrying Battery Packs

Sandilya Kambampati[1]

University of California San Diego, San Diego, CA 92093, USA

Justin S. Gray[2]

NASA Glenn Research Center, Cleveland, OH 44135, USA

H. Alicia Kim[3]

University of California San Diego, San Diego, CA 92093, USA; Cardiff University, Cardiff, CF24 3AA, UK

Abstract

In this study, the optimum design of load carrying battery packs that can also exchange heat with a coolant is presented. The level set topology optimization method is used as the design tool. The flow is modeled using the Darcy potential flow, and the heat transfer is modeled using the convection-diffusion equation. The displacement field is computed using a thermo-elasticity model. A multi-objective optimization is used that minimizes a linear combination of structural compliance, average temperature of the battery cells, and the pressure drop across the coolant. As numerical examples, we present a design study of a load carrying battery pack module that is placed inside an aircraft wing. The efficiency of the optimized designs are demonstrated by showcasing their multifunctional nature—they reduce the temperature in the battery cells by exchanging the heat generated with a coolant all the while sustaining a given load.

[1]Postdoctoral Researcher, Structural Engineering, sandilya.kambampati@gmail.com
[2]Research Engineer, justin.s.gray@nasa.gov
[3]Jacobs Scholars Chair Professor, Structural Engineering, alicia@ucsd.edu

1. Introduction

Multifunctional heat exchangers, such as battery packs that can carry loads and dissipate heat are attractive in electric vehicle design. The battery pack structures in high temperatures are prone to failure due to the high thermo-mechanical loads. In addition, the battery cells can experience thermal runway if the working temperature of the battery exceeds the limit. Improving the efficiency of the designs of battery modules through optimization has been gaining attention recently. Such efficient light weight battery pack modules can improve the fuel efficiency of electric vehicles. The optimization study of air cooled battery packs is presented in [1]. The design was optimized for improving the average temperature and temperature difference, and the design variables are air inlet/outlet angles and the width of the airflow channels between battery cells. The cell spacing of a battery pack module was optimized for lower temperature and more uniform temperature distribution in [2]. In [3], the optimization study of the mechanical features of a battery pack enclosure is presented. A multi-objective function considering a linear combination of mass, frequency, and displacement was optimized using the wall thicknesses as the design variables. The above studies focus on either thermal optimization (temperature based objective functions) or mechanical optimization (displacement or frequency based objective functions). Considering both the mechanical and thermal considerations in the design process can significantly improve the efficiency by yielding multifunctional designs. Specifically, this can circumvent the need for having two separate components: one designed for mechanical considerations such as load bearing properties, and one designed for thermal considerations such as heat dissipation properties. Instead, a single multifunctional component that is designed considering both mechanical and thermal considerations can lead to significant weight savings. The design of such multifunctional battery packs that can exchange heat with a coolant and can carry a load, using level set topology optimization is the focus of this paper.

Topology optimization is an innovative tool used in engineering design for

optimizing multifunctional structures. Topology optimization taking into account multiphysics considerations, particularly thermal properties is challenging owing to the design-dependent nature of the thermal loading. Rodrigues and Fernandes [4] used a material distribution approach to optimize the topology of a 2D solid subject to an increase in temperature. Xia and Wang [5] optimized the topology of a structure subject to an increase in temperature by minimizing the compliance subject to a volume constraint. Gao and Zhang [6] penalized the thermal stress coefficient for topology optimization under thermo-elastic stress loads for minimum compliance. Deaton and Grandhi presented a study on stress-based design of thermal structures in [7], where they explored different objective and constraint functions including mass minimization subject to a stress constraint. Takalloozadeh and Yoon [8] presented a study on a topological derivative formulation for stress minimization problems considering thermo-elastic loading. In these studies, the temperature was assumed to be constant and independent of the design.

In reality, however, the temperature distribution of a structure is dependent on the design, due to heat conduction inside the structure. Li et al. [9] presented a study on the multi-objective optimization for uniform stress and heat flux distributions of a structure. Kruijf et al. [10] studied the influence of heat conduction in both structural and material designs by presenting a multi-objective topology optimization formulation, where two conflicting design criteria—the heat conduction and structural stiffness performances—were optimized. Gao et al. [11] presented a study on the topology optimization of a structure with multiple materials under steady-state temperature and mechanical loading by minimizing the compliance subject to a mass constraint. Kang and James [12] presented multimaterial topology optimization with elastic and thermal response considerations, where they conducted parallel uncoupled finite element analyses to simulate the elastic and thermal response of the structure. Zhu et al. [13] presented a study on topology optimization of coupled thermo-mechanical problems by minimizing the compliance of a structure subject to volume and temperature constraints. However, in the above studies, the heat

flux due to convection is not considered.

Heat exchanger designs commonly incorporate a cooling fluid that flows through the domain for exchanging heat with the solid through convection. Typically, high fidelity turbulent models are used to compute fluid velocity and pressure fields, and convective heat transfer simulation models based on the fluid velocity are used to compute the temperature field. Such high fidelity turbulent models involve solving for computationally expensive non-linearity. Therefore, a lower fidelity model that can reasonably approximate the high fidelity model, is attractive in early conceptual design studies using topology optimization. Recently, a low fidelity flow model for topology optimization is proposed in [14] based on the Darcy potential flow. In [15], the authors showed that the Darcy flow model is a low-fidelity alternative to a turbulent flow model in the design of well-performing cooling channels. Specifically, they showed that for certain geometries, for Reynolds number value of up to 10^4, and when a maximum length scale constraint is imposed on the channel width, the Darcy flow model is a viable alternative for designing cooling channels. A comprehensive review of topology optimization methods for flow based heat transfer problems can be found in [16].

In this paper, we present the design study of multifunctional battery pack structures using level set topology optimization under multiphysics considerations. The topology of the structure is optimized to simultaneously carry a load and to exchange heat with a coolant passing though the structure. The flow is computed using Darcy potential flow, modeled using the finite element method. With the resulting fluid flow, the temperature field is modeled by the convection-diffusion equation using the finite element method. The temperature field is then used in a thermo-elastic model to compute the displacement field. A multiobjective function that is a linear combination of structural compliance, average temperature of the battery cells, and pressure drop across the inlet and outlet of the coolant is minimized. As numerical examples, we present a case study of a battery pack module that is designed to carry a load inside an aircraft wing. To the best of our knowledge, studies on the topology optimiza-

tion of battery packs taking into account coupled structural, thermal, and flow considerations are not found in literature.

2. Optimization Method

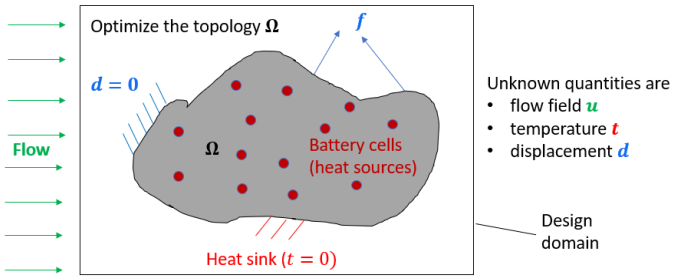

Figure 1: A schematic of the structure subjected to mechanical and thermal loads. The structure also exchanges heat with a coolant.

A schematic illustration of the design domain is shown in Figure 1. The structure (topology is Ω) is subjected to structural loads f (shown in blue) and fixed displacement boundary conditions ($d = 0$). The battery cells (shown in red) are modeled as heat sources and the structure is attached to a heat sink where a zero temperature boundary condition is applied ($t = 0$). A cooling fluid enters the design domain (shown in green) that flows around the structure to enhance the heat transfer. The topology Ω is described and iteratively updated implicitly using the level set function (discussed in Section 2.1). The flow field u, temperature field t, and displacement field d are computed using a flow model, heat transfer model, and a thermo-elastic model (discussed in Section 2.2). The optimization problem formulation is presented in Section 2.3 and the sensitivity computation is discussed in Section 2.4.

2.1. Level Set Method

In this study, the level set method (LSM) is used for topology optimization. The boundary of the structure is described by an implicit function $\phi(x)$, given

by

$$\begin{aligned} \phi(x) &\geq 0, \ x \in \Omega \\ \phi(x) &= 0, \ x \in \Gamma \\ \phi(x) &< 0, \ x \notin \Omega \end{aligned} \tag{1}$$

where Ω is the topology of the domain, Γ is the domain boundary. The boundary of the structure is defined implicitly through $\phi(x)$, allowing the boundary to change under a given velocity field $V_n(x)$, using the level set equation given by [17],

$$\frac{d\phi(x)}{dt} + |\nabla\phi(x)|V_n(x) = 0, \tag{2}$$

which is discretized and solved numerically using the following equation [18],

$$\phi_j^{k+1} = \phi_j^k - \Delta t|\nabla\phi_j^k|V_{n,j} \tag{3}$$

where j is a discrete point in the domain, and $|\nabla\phi_j|$ is the norm of the gradient, computed using the Hamilton-Jacobi weighted essentially non-oscillatory (HJ-WENO) scheme [17]. We note that the level set equation defined in Eq. (2) can modify topology by merging holes, but it cannot create holes in the interior of the solid. However, the level set equation can be augmented with hole creation algorithms [19] for seeding new holes during the topology optimization process.

For a given topology, the boundary is extracted as a set of boundary points, and the fractions of the elemental volume cut by the level set for all the finite elements are computed. This is followed by a finite element analysis and element centroid sensitivity computation. The boundary point sensitivities are computed from the element centroid sensitivities using the least squares interpolation method. Using the sensitivities, the boundary point velocities are optimized using mathematical programming. The level set function is then updated using the boundary point velocity.

2.2. Multiphysics Model

A schematic of the multiphysics model is shown in Figure 2. The model begins with the flow solver (the green box) computing the fluid velocity in the

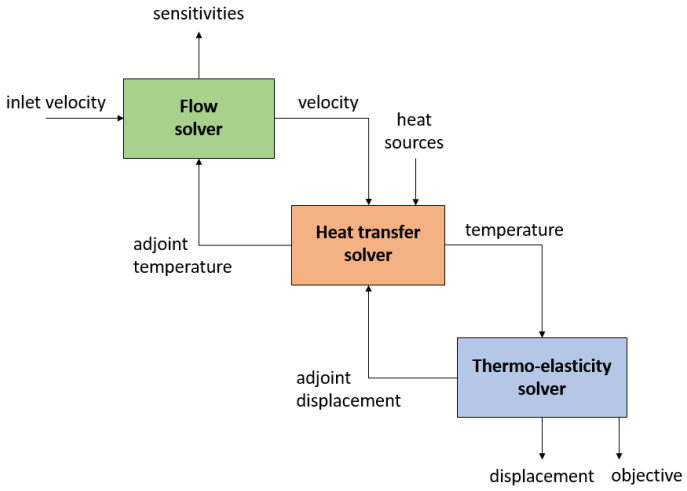

Figure 2: A modular description of the mathematical models developed in house in this study. The flow solver computes the flow field, the heat transfer solver computes the temperature considering convection, and the thermo-elasticity solver computes the displacement field.

domain. The heat transfer solver (the orange box) assembles the heat load resulting from the heat sources and the convective heat flux from the velocity field, and computes the temperature distribution in the domain. The thermo-elasticity solver (the blue box) computes the displacement field in the domain while taking into account the thermal strain caused by the temperature field. The thermo-elasticity solver computes the adjoint state displacement, which is passed to the temperature solver for computing the adjoint state temperature. Finally, the sensitivities are computed using the state and adjoint state variables. A detailed description of the flow, temperature, and thermo-elasticity models are presented in the following sections.

2.2.1. Fluid Flow Model

A common model used to describe internal flows is the incompressible steady state Navier-Stokes equations given by

$$\rho u \cdot \nabla u = -\nabla p + \mu \nabla^2 u \tag{4}$$

$$\nabla \cdot u = 0 \tag{5}$$

where ρ is the density, u is the velocity of the fluid, μ is the dynamic viscosity, and p is the pressure . The Navier-Stokes equations are non-linear equations, and typically turbulence models such as Reynolds-Averaged Navier-Stokes (RANS) simulations are used to model this flow. However, the computational cost of simulating RANS equations is high. A low-fidelity alternative to the RANS model is to use the Darcy potential flow [14], which assumes the velocity to be proportional to the gradient of pressure as

$$u = -\frac{\kappa}{\mu}\nabla p \tag{6}$$

where κ is the permeability of the fluid. Eq. (6) is substituted in the continuity equation in Eq. (5) yielding

$$\nabla \cdot (\frac{\kappa}{\mu}\nabla p) = 0 \tag{7}$$

The above equation is a linear partial differential equation, which is significantly easier to compute than the RANS equations. The Darcy potential flow is a viable low fidelity approximation to simulate the flow field when the channel width is small [15]. The finite element method is used to model the Darcy potential flow in Eq. (7), given by

$$K_p p = f_p \tag{8}$$

where N_e is the number of elements, K_p is the permeability matrix, given by

$$K_p = \sum_{i}^{N_e} K^e_{p,i} \tag{9}$$

$K^e_{p,i} = \kappa_i/\mu K^e_{p,0}$ is the elemental permeability matrix, and

$$K^e_{p,0} = \int_{\Omega_i} B^T B d\Omega \tag{10}$$

is the homogeneous elemental permeability matrix, $B = \nabla N$ is the gradient of the shape functions N, and

$$\kappa_i = \kappa_s + (\kappa_f - \kappa_s)x_i \tag{11}$$

where x_i is the fraction of the elemental volume cut by the level set, κ_s and κ_f are the permeability values of the solid and fluid, respectively, and Ω_i is the domain of the element i. The right hand side of Eq. (8), f_p is given by

$$f_p = \int_\Gamma N^T (n \cdot u_{in}) d\Gamma \tag{12}$$

where u_{in} is velocity of the flow at the inlet, and n is the normal vector to the boundary.

2.2.2. Heat Transfer Model

Based on the fluid velocity u, the heat transfer can be modeled using the following convection-diffusion equation

$$\rho c_p u \cdot \nabla t = k \nabla^2 t + q \tag{13}$$

where k is the conductivity coefficient, c_p is the specific heat, t is temperature, and q is the heat generation rate. The finite element analysis can be used to model Eq. (13) as

$$(K_t + C)t = f_t \tag{14}$$

where K_t is the conductivity matrix, C is the convection matrix, and f_t is the thermal load. The conductivity matrix K_t is approximated by

$$K_t = \sum_i^{N_e} K_{t,i}^e = \sum_i^{N_e} (k_s + (k_f - k_s) x_i) K_{t,0}^e \tag{15}$$

where k_s is the conductivity of the solid, k_f is the conductivity of the fluid, and $K_{t,0}^e$ is the homogeneous elemental conduction matrix is given by

$$K_{t,0}^e = \int_{\Omega_i} B^T B d\Omega \tag{16}$$

The convection matrix C is assembled using the following elemental convection matrix C^e, given by

$$C = \sum_i^{N_e} C^e = \sum_i^{N_e} \rho_i c_{p,i} \kappa_i C_0^e \tag{17}$$

where $c_{p,i}$ and ρ_i are interpolated elemental density and specific heat coefficient, given by

$$\rho_i = \rho_s + (\rho_f - \rho_s) x_i \tag{18}$$

$$c_{p,i} = c_{ps} + (c_{pf} - c_{ps})x_i \tag{19}$$

where ρ_s and ρ_f are the densities of solid and fluid, respectively, c_{ps} and c_{pf} are the specific heat coefficients of solid and fluid, respectively, and C_0^e is the homogeneous elemental convection matrix given by

$$C_0^e = \int_{\Omega_i} -\hat{N}^T (\frac{1}{\mu} B p_e)^T B d\Omega \tag{20}$$

where p_e are the pressure values at the element nodes, and $\hat{N}$ includes the streamline upwind stabilization term given by

$$\hat{N} = N + \frac{h_e}{2} \left(\frac{u}{\|u\|} \right) B \tag{21}$$

where h_e is the width of an element.

2.2.3. Thermo-Elastic Model

A variation of temperature causes a structure to expand or contract, resulting in thermal strain ϵ_t. Specifically, the strain $\epsilon_{t,i}$ of an element i caused by the temperature change is given by

$$\epsilon_{t,i} = \alpha_i t_i \tag{22}$$

where $\alpha_i = x_i \alpha$ is the coefficient of the linear expansion of element i, α is the coefficient of linear expansion of the solid material, and t_i is the temperature change of the element. The elemental strain is imposed on the element as a thermo-elastic force f_{ti}^e, given by

$$f_{ti}^e = H_i^e t_i^e \tag{23}$$

where t_i^e is the temperature change at the nodes of an element i, and H_i^e is the elemental thermo-elastic force generating matrix given by

$$H_i^e = x_i H_0^e \tag{24}$$

where

$$H_0^e = \int_{\Omega_i} \alpha B_s^T C \epsilon^e N_s d\Omega \tag{25}$$

and B_s is the gradient of the displacement shape function matrix N_s, C is the elasticity tensor, and ϵ^e is a unit principal strain. The elemental thermo-elastic force is then assembled to form the global thermo-elastic force f_t as

$$f_t = \sum_{i=1}^{N_e} f_{ti}^e = Ht \tag{26}$$

where H is the matrix that assembles the thermo-elastic force from a given temperature distribution given by

$$H = \sum_{i}^{N_e} H_i^e \tag{27}$$

The thermo-elastic force is added to the mechanical force f_m, and used in the following equation is used to compute the displacement d under mechanical and thermal loads

$$K_s d = f_m + f_t = f_m + Ht \tag{28}$$

where K_s is the structural stiffness matrix of the structure, given by

$$K_s = \sum_{i=1}^{N_e} K_{si}^e = \sum_{i=1}^{N_e} E_i K_{s0}^e \tag{29}$$

where $K_{si}^e = E_i K_{s0}^e$ is the elemental stiffness matrix of element i, and K_{s0}^e is the homogeneous elemental stiffness matrix, given by

$$K_{s0}^e = \int_{\Omega_i} B_s^T C B_s d\Omega \tag{30}$$

and E_i and E are the elasticity moduli of the element and the material, given by

$$E_i = E_{min} + (E - E_{min}) x_i \tag{31}$$

where E_{min} is the elasticity modulus of the void region.

2.3. Optimization problem formulation

The objective of this study is to solve the following multi-objective problem

$$\begin{aligned} \min_{\Omega} \quad & J = k_c C/C_0 + k_t T_{av}/T_0 + k_p P_d/P_0 \\ \text{subject to} \quad & K_p p = f_p \\ & (K_t + C)t = f_t \\ & K_s d = f_m + Ht \\ & V \leq V_0 \\ & \max r \leq r_{max} \end{aligned} \tag{32}$$

where C is the compliance, and T_{av} is the average temperature of the battery cells, and P_d is the pressure drop. k_c, k_t, and k_p are the weights for compliance, average temperature, and pressure drop, respectively. C_0, T_0, P_0 are reference compliance, temperature, and pressure used to non-dimensionalize the objective function. The volume of the topology and volume constraint used on the topology are V and V_0, respectively. r is the maximum radius of the flow channels, and r_{max} is the maximum length scale constraint. The flow state equations, temperature state equations, and the thermo-elasticity state equations are included as equality constraints in the optimization formulation in Eq. (32). The objective and constraint functions are linearized using the boundary point sensitivities. The optimization problem solved using the sequential linear programming and the Simplex method, implemented using the GLPK library (gnu.org/software/glpk/). Further details on our level set topology optimization algorithm can be found in [20].

2.4. Sensitivity computation

In this section, the computations of the boundary point sensitivities for compliance, average temperature, and pressure using the adjoint state method are presented. First, the sensitivities are calculated at the centroids of all the elements from which the boundary point sensitivities are determined using the least squares interpolation [21]. The element centroid sensitivity of a function of interest J is defined as dJ/dx, where x is the volume fraction of the element.

2.4.1. Compliance sensitivities

The compliance of the structure under thermal and mechanical loads is given by

$$C = d^T K_s d = f^T d = (f_m + Ht)^T d \tag{33}$$

The Lagrangian function $\mathcal{L}$ of the compliance is defined as

$$\mathcal{L} = (f_m + Ht)^T d + \lambda_d^T (f_m + Ht - K_s d) + \lambda_t^T (f_t - K_t t) + \lambda_p^T (f_p - K_p p) \tag{34}$$

where λ_d, λ_t, and λ_p are the adjoint state variables corresponding to structural displacement d, temperature t, and pressure p. λ_d is computed by solving $\frac{\partial \mathcal{L}}{\partial d} = 0$, which yields

$$f^T - \lambda_d^T K_s = 0 \tag{35}$$

The adjoint state variable λ_t is computed by solving $\frac{\partial \mathcal{L}}{\partial t} = 0$, which yields

$$(K_t^T + C^T)\lambda_t = -\lambda_d H - d^T H \tag{36}$$

The adjoint state variable λ_p is computed by solving $\frac{\partial \mathcal{L}}{\partial p} = 0$, resulting in

$$K_p \lambda_p = -t^T \frac{\partial C}{\partial p} \lambda_t \tag{37}$$

The Lagrangian function $\mathcal{L}$ is differentiated with respect to the volume fraction x_i of each element to compute the elemental centroid sensitivities of compliance s_i, given by

$$\begin{aligned}
s_i &= \frac{\partial \mathcal{L}}{\partial x_i} \\
&= \frac{\partial}{\partial x_i} \left((f_m + Ht)^T d + \lambda_d^T (f_m + Ht - K_s d) + \lambda_t^T (f_t - K_t t) + \lambda_p^T (f_p - K_p p) \right) \\
&= t^T \frac{\partial H}{\partial x_i} d + \lambda_d^T \frac{\partial H}{\partial x_i} t - \lambda_d^T \frac{\partial K_s}{\partial x_i} d - \lambda_t^T \frac{\partial K_s}{\partial x_i} t - \lambda_p^T \frac{\partial K_p}{\partial x_i} p \\
&= t_i^{eT} H_0^e d_i^e + \lambda_{di}^{eT} H_0^e t_i^e - \lambda_{di}^{eT} K_{s0}^e d_i^e - \lambda_{ti}^{eT} K_{t0}^e t_i^e - \lambda_{pi}^{eT} K_{p0}^e p_i^e
\end{aligned} \tag{38}$$

where λ_{di}^e, λ_{ti}^e, and λ_{pi}^e are the adjoint state variables of displacement, temperature, and pressure at the element nodes, respectively, d_i^e, t_i^e, and p_i^e are the displacement, temperature, and pressure values at the nodes, respectively.

2.4.2. Average temperature sensitivities

The average temperature T_{av} is given by

$$T_{av} = f_1^T t \tag{39}$$

where f_1 is a vector with all its elements set to 0, except for the nodes located at the center of the battery cells, whose values are set to $1/N_c$ (where N_c is the number of battery cells). The Lagrangian function $\mathcal{L}$ is given by

$$\mathcal{L} = f_1^T t - \lambda_t^T((K_t + C)t - f_t) - \lambda_p^T(K_p p - f_p) \tag{40}$$

where λ_t and λ_p are the adjoint state variables corresponding to the temperature and flow variables. The adjoint state variable λ_t is computed by solving $\frac{\partial \mathcal{L}}{\partial t} = 0$, which yields

$$(K_t^T + C^T)\lambda_t = f_1 \tag{41}$$

The adjoint state variable λ_p is computed by solving $\frac{\partial \mathcal{L}}{\partial p} = 0$, resulting in

$$K_p \lambda_p = f_2 - t^T \frac{\partial C}{\partial p}\lambda_t \tag{42}$$

Note that the term $\frac{\partial C}{\partial p}$ appears in Eq. (42) because the convection matrix depends on the flow velocity.

The Lagrangian function $\mathcal{L}$ can be differentiated with respect to the volume fraction x_i of an element i to compute the sensitivity at the centroid s_i as following

$$\begin{aligned}
s_i &= \frac{\partial \mathcal{L}}{\partial x_i} \\
&= \frac{\partial}{\partial x_i}\left(f_1^T t - \lambda_t^T((K_t + C)t - f_t) - \lambda_p^T(K_p p - f_p)\right) \\
&= -\lambda_t^T\left(\frac{\partial K_t}{\partial x_i} + \frac{\partial C}{\partial x_i}\right)t - \lambda_p^T \frac{\partial K_p}{\partial x_i} p \\
&= -(k_f - k_s)\lambda_{t,i}^{eT} K_{t,0}^e t_i^{eT} \\
&\quad - \left[\rho_i c_{p,i}(\kappa_f - \kappa_s) + \kappa_i c_{p,i}(\rho_f - \rho_s) + \rho_i \kappa_i (c_{pf} - c_{ps})\right] \lambda_{t,i}^{eT} C_0 t_i^{eT} \\
&\quad -(\kappa_f - \kappa_s)\lambda_{p,i}^{eT} K_{p,0}^e p_i^{eT}
\end{aligned} \tag{43}$$

2.4.3. Pressure drop sensitivities

The pressure drop P_d is given by

$$P_d = f_2^T p \tag{44}$$

where f_2 is a vector with all its elements set to 0, except for the nodes located at the outlets, whose values are set to $1/N_p$ (where N_p is the number of outlet nodes). The Lagrangian function $\mathcal{L}$ is given by

$$\mathcal{L} = f_2^T p - \lambda_p^T (K_p p - f_p) \tag{45}$$

where λ_p is the adjoint state variable for pressure, solving $\frac{\partial \mathcal{L}}{\partial p} = 0$, resulting in

$$K_p^T \lambda_p = f_2 \tag{46}$$

The elemental centroid sensitivities of pressure s_i, the Lagrangian function $\mathcal{L}$ is differentiated with respect to the volume fraction x_i of each element, given by

$$\begin{aligned} s_i &= \frac{\partial \mathcal{L}}{\partial x_i} \\ &= -(\kappa_f - \kappa_s) \lambda_{p,i}^{eT} K_{p,0}^e p_i^{eT} \end{aligned} \tag{47}$$

We note that the coupled multiphysics problem presented in this paper exhibits a linear, one-way coupling. Specifically, the flow affects the temperature distribution, and the temperature does not affect the flow. Similarly, the temperature affects the displacement fields, while the displacement field does not affect temperature. Considering the two-way coupled problem, where the flow, temperature, and displacement fields affect each other is significantly challenging and beyond the scope of this paper.

3. Numerical Examples

In this section, the numerical examples for the design of a battery pack module are presented. Such battery packs are commonly used in electric aircraft such as the NASA's X-57 "Maxwell" aircraft [22]. A schematic of the battery pack module is shown in Figure 3. The battery modules are assumed to be

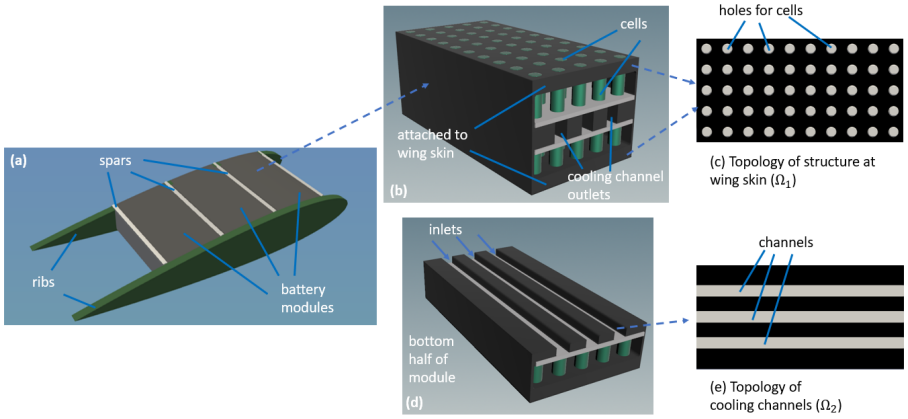

Figure 3: A schematic of the battery modules placed between adjacent ribs and spars. Each module consists of two rows of battery cells and cooling channels pass through the module between the rows of battery cells.

stacked between adjacent ribs and spars of the wing as shown in Figure 3a. The side walls of the battery pack modules can also act as spars. Each battery pack module has two rows of battery cells on top and bottom, with each row having a total of fifty battery cells as shown in Figure 3b. The battery module's top and bottom regions are attached to the wing skin. The topologies of the battery module at the top and bottom that hold the battery cells in place (shown in Figure 3c) are modeled as extruded 2D topologies (Ω_1). The module has cooling channels running through the mid plane, between the two rows of battery cells as shown in Figure 3d. The cooling channels are modeled as extruded 2D topologies (Ω_2) as shown in Figure 3e. The design is modeled using extruded 2D topologies for ease of manufacturing.

3.1. Problem setting

In this section, the problem setting used for the topology optimization of the battery module is presented. Specifically, we present the results for the design of one battery module located at the root of wing. The dimensions of the battery module are 0.4 m in the spanwise direction, 0.2 m in the chordwise direction, and 0.16 m in the thickness direction (Figure 4). The battery module

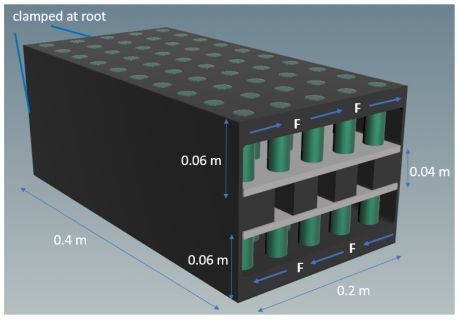

Figure 4: Dimensions of the battery module and boundary conditions.

material is made of aluminum. The wing is assumed to have same dimensions as that of the Cessna 172 aircraft, which has a gross weight of $1.1\times\ 10^3$ kg (2450 lbs) [23]. The module is designed for a 2.5g torsional load case. Assuming the distance between the elastic axis and aerodynamic center of the wing to be approximately 5% of the chord, the root torsional moment is computed to be approximately 680 Nm. This torsion load is applied as shear loads along the top and bottom of one side of the battery pack, and clamped on the other side, as shown in Figure 4.

Each battery cell (diameter of 18 mm and height of 650 mm) produces a heat load $q = 0.5$ W. The battery cell has a conductivity coefficient $\kappa_r = 0.434$ W/m/K in the radial direction and $\kappa_a = 2.17$ W/m/K in the axial direction [24]. The coolant (water) enters the design domain at 20 ^{o}C at the inlets with a velocity of 1 m/s (flow rate of 0.64 m^3/s). The properties of all the materials used in this study are shown in Table 1.

The objective is to minimize the multi-objective function $J = k_c C/C_0 + k_t T_{av}/T_0 + k_p P_d/P_0$, where C, T_{av}, and P_d are the compliance, average temperature, and pressure drop, respectively, and k_c, k_t, and k_p are the corresponding weights. The design variable is the topology $\Omega = \Omega_1 \cup \Omega_2$, where Ω_1 is the topology of the structure near the wing skin (Figure 3c) and Ω_2 topology of the cooling channels (Figure 3e). The volume constraint used is $V_0 = 50\%$, and the maximum channel length scale constraint $r_{max} = 0.02$ m is used. A 3D finite

element mesh comprising of $200 \times 100 \times 80$ cubic elements in the chordwise, spanwise, and thickness direction, respectively, is used for the analysis. The extraction of the 2D boundary sensitivities of topologies Ω_1 and Ω_2 from the 3D sensitivity distribution is explained in Appendix-A.

Table 1: Material properties used in this study.

ine			
	Water	Aluminum	Battery
ine			
Conductivity (k, W/m/K)	0.6	237.0	2.17 (axial)
			0.434 (radial)
Density (ρ , kg/m^3)	1000.0	2700.0	2700.0
Viscosity (μ, Pa s)	0.001	–	–
Permeability (m^2)	2.5×10^{-6}	–	–
Elastic modulus (GPa)	–	69.0	–
Poisson's ratio	–	0.3	–
ine			

3.2. Results

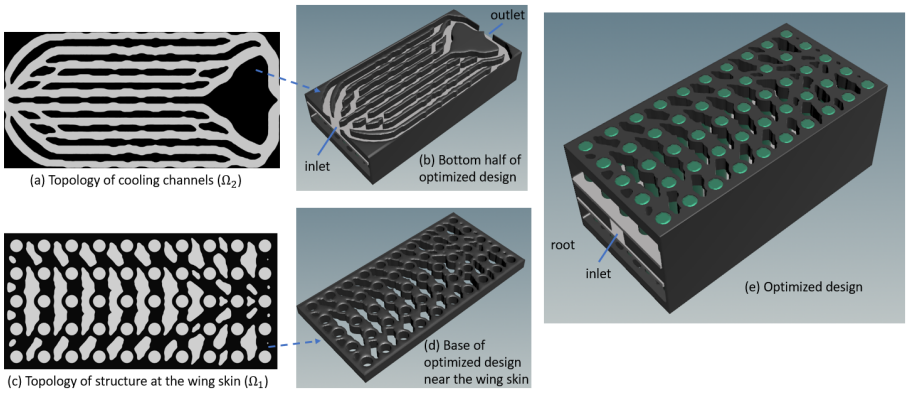

Figure 5: The optimized design of the battery module obtained for $k_p = k_t = k_c = 0.33$.

In this section, the optimization results for different values of k_c, k_p, and k_t are presented. The reference values used are $P_0 = 2.0$ Pa, $T_0 = 1.0\ ^oC$ and $C_0 = 0.025$ Nm. Figure 5 shows the results for $k_c = k_p = k_t = 0.33$. In Figure 5a the topology of the cooling channels (Ω_2) is shown. We can see that the channels are distributed in such a way that the fluid enters the domain, travels to different regions drawing heat from the solid while it travels, and exits through the outlet. The bottom half of the battery module is shown in Figure 5b for visualizing the cooling channels that run through the module. The topology of the structure at the top and bottom of the module (Ω_1) is shown in Figure 5c and a 3D view is shown in Figure 5d. The complete optimized battery module is shown in Figure 5e.

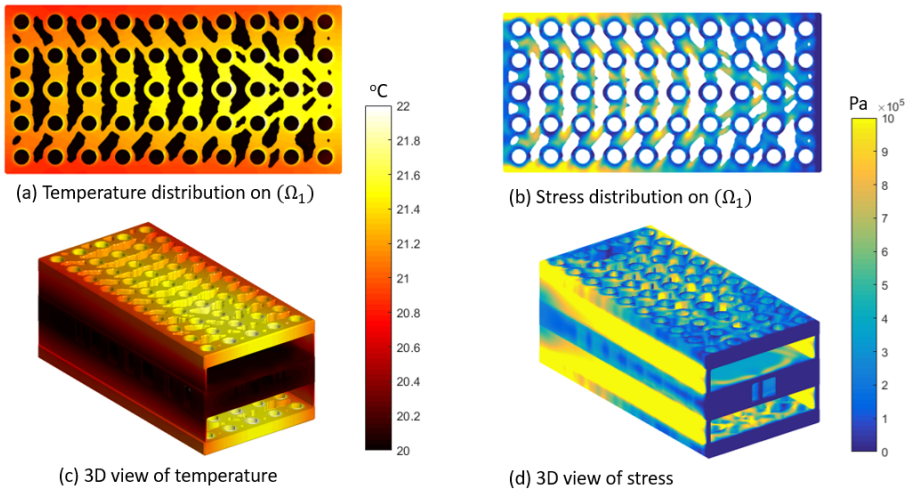

Figure 6: The temperature and stress distribution on the structure. The results show the multi-functional nature of the battery pack module showing the structure can diffuse heat as seen by the temperature gradients, and can also carry a load as seen by the stress distribution.

Figure 6 shows the optimized stress and temperature. Figure 6 illustrates the multi-functional nature of the optimized design. The structure around the battery pack diffuses the heat generated from the batteries via conduction, as evidenced by the temperature gradient in Figures 6a and 6c. The structure also carries load, as evidenced by the stress distribution in Figure 6b.

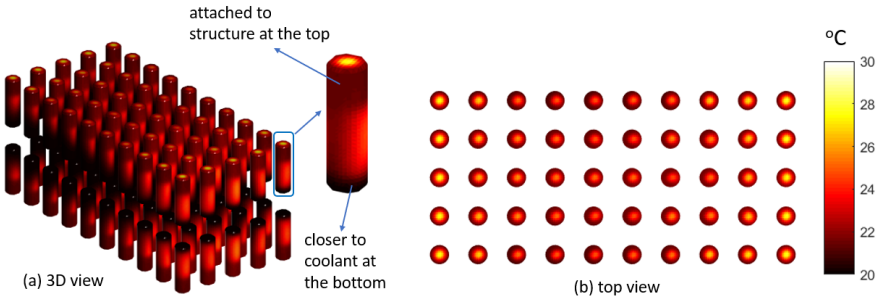

Figure 7: The temperature distribution of the battery cells. A close-up view of the battery cell in the corner shows that the battery cell is the coolest at its bottom where it is near the coolant; and is hottest in the interior of the battery cell. (b) The cells towards the outer edges are hotter than the cells in the interior.

The temperature distribution of the battery cells is shown in Figure 7. A 3D view of the temperature in the cells is shown in Figure 7a. Examining the close-up view of the battery cell in the corner, where we can see that the temperature is high in the interior of the battery cell, and the temperature is the lowest at the bottom where is it closest to the coolant. The top view of the temperature distribution is shown in Figure 7b, where we can see that the temperatures of the cells are high on the outer regions of the module and lower for cells in the interior.

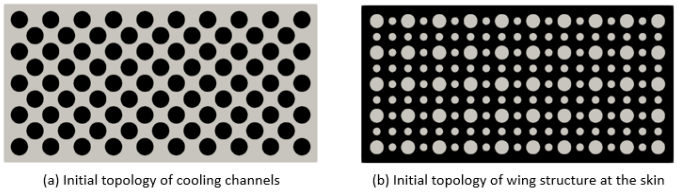

Figure 8: The initial topologies used in the optimization for (a) cooling channels and (b) structure at the wing skin.

The initial topologies used in the optimization are generated using spatially distributed holes for both the cooling channels and the structure, as shown in Figure 8. The iteration history of the objective function J and the volume V is shown in Figure 9. The optimization is run for a total of 160 iterations.

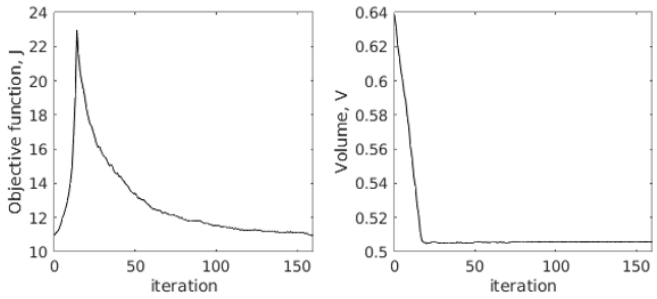

Figure 9: The optimization history of the objective function J and the volume V.

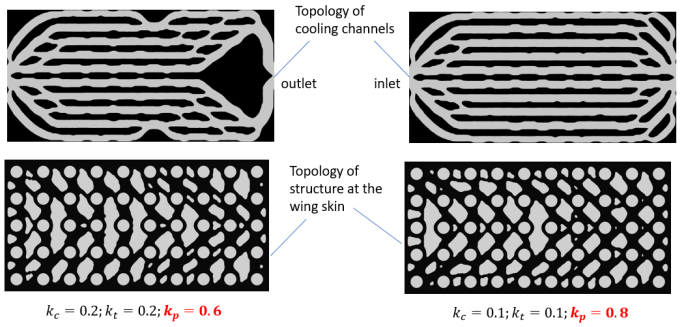

Figure 10: The optimized topologies obtained for ($k_c = k_t = 0.2, k_p = 0.6$) and ($k_c = k_t = 0.1, k_p = 0.8$).

The optimization results for other values of the multi-objective weights k_c, k_t, and k_p are discussed here. In Figure 10, the optimization results when higher values are used for weight for pressure ($k_p = 0.6$ and 0.8) and lower weight values for temperature and compliance ($k_c = k_t = 0.2$, and $k_c = k_t = 0.1$) are shown in Figure 10. We can see from Figure 10 that as k_p increases from 0.6 to 0.8, the optimized topology of the cooling channels changes significantly at the region close to outlet on the right—from oblique channels for $k_p = 0.6$ to straight horizontal channels for $k_p = 0.8$.

In Figure 11, the optimization results obtained when higher values are used for the weight for compliance ($k_c = 0.6$ and 0.8) and lower weight values for temperature and pressure ($k_p = k_t = 0.2$, and $k_p = k_t = 0.1$) are shown in Figure 11. We can see that changing the weight for the compliance from k_c

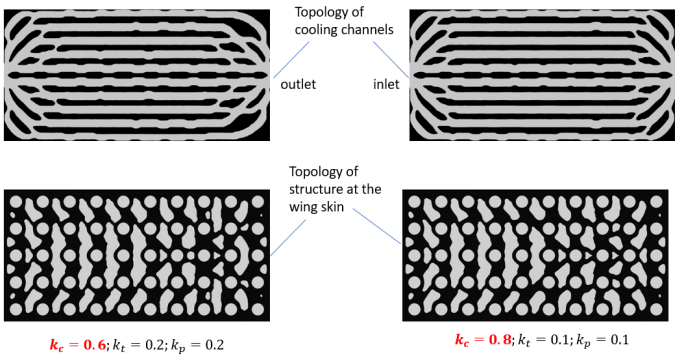

Figure 11: The optimized topologies obtained for $(k_p = k_t = 0.2, k_c = 0.6)$ and $(k_p = k_t = 0.1, k_c = 0.8)$.

$= 0.6$ to 0.8 has a negligible effect on the optimized topology of the cooling channels.

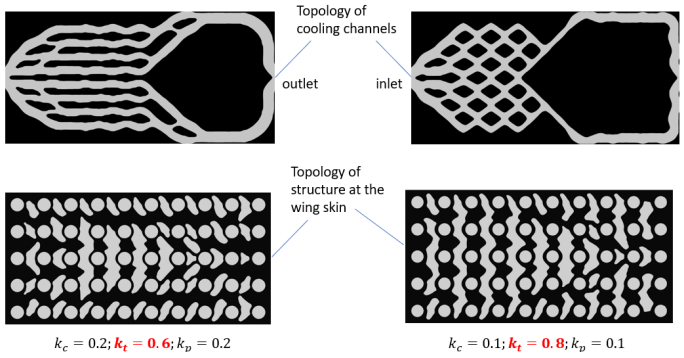

Figure 12: The optimized topologies obtained for $(k_c = k_p = 0.2, k_t = 0.6)$ and $(k_c = k_p = 0.1, k_t = 0.8)$.

Figure 12 shows the optimization results when the higher values are used for the weight for temperature ($k_t = 0.6$ and 0.8) and lower weight values for compliance and pressure ($k_c = k_p = 0.2$, and $k_c = k_p = 0.1$) are shown in Figure 11. We can see that changing the weight for the temperature from $k_t = 0.6$ to 0.8 has a significant effect on the optimized topology of the cooling channels – with the flow being directed towards the corners on the right side before merging at the outlet.

Table 2: Optimized pressure, temperature, and compliance values for different values of k_p, k_c, and k_t.

	k_c	k_t	k_p	C/C_0	T_{av}/T_0	P_d/P_0
(a)	0.33	0.33	0.33	1.0	12.5	19.5
(b)	0.2	0.2	0.6	2.4	12.7	6.5
	0.1	0.1	0.8	5.7	13.4	1.8
(c)	0.6	0.2	0.2	0.3	13.5	41.6
	0.8	0.1	0.1	0.1	13.5	109.0
(d)	0.2	0.6	0.2	1.1	11.1	26.9
	0.1	0.8	0.1	1.5	8.1	44.8

Table 2 shows the normalized optimum compliance, temperature, and pressure values obtained for different values of k_c. k_t, and k_p. In Table 2a the results obtained when all the weights are the same, $k_t = k_p = k_c = 0.33$ are shown (topologies shown in Figure 5). For the sake of comparison, we refer to the optimum normalized compliance, average temperature, and pressure drop values in Table 2a as the baseline values.

Table 2b shows the results obtained when more weight is given to the pressure than the baseline, with $k_p = 0.6$, 0.8 (topologies shown in Figure 10). The optimized pressure values are significantly reduced compared to the baseline pressure ($P_d/P_0 = 6.5$, 1.8). There is also a significant increase in the compliance, ($C/C_0 = 2.4$, 5.7), but only a modest increase in the temperature ($T/T_{av} = 12.7$, 13.4).

Table 2c shows the results obtained the weight corresponding to compliance is the highest, $k_c = 0.6$, 0.8 (topologies shown in Figure 11). The corresponding optimized normalized compliance values are significantly smaller than the baseline ($C/C_0 = 0.3$, 0.1) and the normalized pressure significantly increases

($P_d/P_0 = 41.6, 109.0$) compared to the baseline. The average temperature increases modestly to ($T/T_{av} = 13.5$, 13.5) compared to the baseline.

Table 2d shows the results obtained the weight corresponding to the average temperature is the highest, $k_t = 0.6$, 0.8 (topologies shown in Figure 12). The corresponding optimized normalized average temperature values reduce to ($T_{av}/T_0 = 11.1$, 8.1) compared to the baseline. The compliance and pressure increase to ($P_d/P_0 = 26.9$, 44.8) and ($C/C_0 = 1.1$, 1.5) compared to the baseline.

We note from Table 2 that pressure drop values in the designs can range from a low $P_d/P_0 = 1.8$ to a high $P_d/P_0 = 109.0$. Comparatively, the average temperature only ranges from $T_{av}/T_0 = 8.1$ to $T_{av}/T_0 = 13.5$. The variation (with respect to k_p, k_c, and k_t) of pressure drop in the designs is observed to be significantly higher compared to the average temperature. This observation can be attributed to the multifunctional nature of the structure. The pressure drop is completely dependent on the cooling channel design, while the temperature is only partially dependent on the cooling channels. Specifically, the batteries dissipate heat via conduction through the structure and via exchanging heat with the flow. Therefore, even if the cooling channel design in inefficient for heat dissipation, the batteries can still dissipate heat via conduction through the solid structure—thus explaining the relatively lower variation in the average temperature observed.

In conclusion, if a designer wants a structure with the most flow efficiency, and is willing to sacrifice stiffness and thermal efficiency, the designs corresponding to Table 2b are the best of the choices, as they have the lowest pressure drop values. Similarly, if a designer wants a stiff structure, and is willing to sacrifice thermal and flow efficiency, the designs corresponding to Table 2c are the best of the choices, as they have the lowest compliance values. Furthermore, if a designer wants a thermally efficient structure, and is willing to sacrifice stiffness and flow efficiency, the designs corresponding to Table 2d are the best of the choices, as they have the lowest temperature values. Finally, if a designer wants a structure with efficient flow, structural, and thermal properties, then the design corresponding to Table 2a offers the best compromise.

4. Conclusion

In this paper, the optimum design study of multifunctional structures that can withstand a load and also exchange heat with a coolant is presented. The level set topology optimization method is used as the design tool. The flow is computed using a Darcy potential flow model, which is used in a heat transfer model to compute the temperature field. A thermo-elasticity model is used to compute the displacement field. A multi-objective function is minimized that is a combination of structural compliance, average temperature in battery cells, and pressure drop across inlet and outlet of the cooling channel.

As numerical examples, we discuss the design of a battery pack module that is placed inside an aircraft wing to carry loads. The optimized structure efficiently reduces the temperature of the battery cells by exchanging the heat generated by the cells with the coolant, while carrying a load. The optimized cooling channels are distributed in such a way that the fluid enters the domain, branches out into different smaller channels for efficient heat transfer at the cost of higher pressure drops. The temperature distribution on the battery cells show that the cells are the coolest near the regions that are closer to the coolant, and are hottest near the regions that are closer to the center of the cell and away from the coolant. The optimization results showcase the multifunctional nature of the optimized designs in terms of efficient heat transfer and load carrying capabilities.

Acknowledgments

The authors acknowledge the support from the NASA's Transformational Tools and Technologies project (grant number 80NSSC18M0153). The authors also acknowledge the support from NSF (grand number 1762530) and EPSRC (grant number EP/M002322/2).

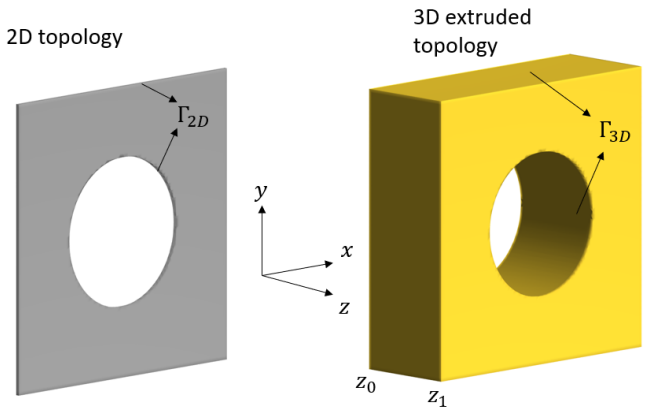

Figure 13: A schematic of a 2D topology and the corresponding extruded 3D topology.

Appendix A Extracting 2D boundary sensitivity

A schematic of a 2D topology in the $x-y$ plane and its corresponding 3D topology extruded in the z direction from $z = z_0$ to $z = z_1$ is shown in Figure 13. The expression for the shape sensitivity for an objective function $J(\Omega)$ under a perturbation field θ is given by [25]

$$J'(\Omega)(\theta) = \int_{\Gamma} s_{3D}(\theta \cdot n)\ d\Gamma_{3D} \tag{48}$$

where s_{3D} is the sensitivity field and n is the boundary normal, and Γ_{3D} is the 3D boundary. For an extruded 3D topology, we have

$$d\Gamma_{3D} = d\Gamma_{2D}\ dz \tag{49}$$

where Γ_{2D} is the boundary of the 2D topology and z is the extrusion direction. Substituting Eq. (49) in Eq. (48), we get the following expression for shape sensitivity

$$\begin{aligned} J'(\Omega)(\theta) &= \int_{\Gamma} s_{3D}(\theta \cdot n)\ d\Gamma_{2D}\ dz \\ &= \int_{\Gamma} \left(\int_{z_0}^{z_1} s_{3D} dz \right) (\theta \cdot n)\ d\Gamma_{2D} \\ &= \int_{\Gamma} s_{2D}(\theta \cdot n)\ d\Gamma_{2D} \end{aligned} \tag{50}$$

where the 2D shape sensitivity is given as

$$s_{2D} = \int_{z_0}^{z_1} s_{3D} dz \tag{51}$$

We note that when the objective function $J(\Omega)$ is volume V, the sensitivity $s_{3D} = 1$ [25]. Therefore, the sensitivity for the volume is given by

$$s_{2D} = \int_{z_0}^{z_1} dz \tag{52}$$

References

[1] J. Xie, Z. Ge, M. Zang, S. Wang, Structural optimization of lithium-ion battery pack with forced air cooling system, Applied Thermal Engineering 126 (2017) 583–593 (2017).

[2] X. Liao, C. Ma, X. Peng, A. Garg, N. Bao, Temperature distribution optimization of an air-cooling lithium-ion battery pack in electric vehicles based on the response surface method, Journal of Electrochemical Energy Conversion and Storage 16 (4) (2019).

[3] L. Shui, F. Chen, A. Garg, X. Peng, N. Bao, J. Zhang, Design optimization of battery pack enclosure for electric vehicle, Structural and Multidisciplinary Optimization 58 (1) (2018) 331–347 (2018).

[4] H. Rodrigues, P. Fernandes, A material based model for topology optimization of thermoelastic structures, International Journal for Numerical Methods in Engineering 38 (12) (1995) 1951–1965 (1995).

[5] Q. Xia, M. Y. Wang, Topology optimization of thermoelastic structures using level set method, Computational Mechanics 42 (6) (2008) 837 (2008).

[6] T. Gao, W. Zhang, Topology optimization involving thermo-elastic stress loads, Structural and multidisciplinary optimization 42 (5) (2010) 725–738 (2010).

[7] J. D. Deaton, R. V. Grandhi, Stress-based design of thermal structures via topology optimization, Structural and Multidisciplinary Optimization 53 (2) (2016) 253–270 (2016).

[8] M. Takalloozadeh, G. H. Yoon, Development of pareto topology optimization considering thermal loads, Computer Methods in Applied Mechanics and Engineering 317 (2017) 554–579 (2017).

[9] Q. Li, G. P. Steven, O. M. Querin, Y. Xie, Structural topology design with multiple thermal criteria, Engineering Computations 17 (6) (2000) 715–734 (2000).

[10] N. de Kruijf, S. Zhou, Q. Li, Y.-W. Mai, Topological design of structures and composite materials with multiobjectives, International Journal of Solids and Structures 44 (22-23) (2007) 7092–7109 (2007).

[11] T. Gao, P. Xu, W. Zhang, Topology optimization of thermo-elastic structures with multiple materials under mass constraint, Computers & Structures 173 (2016) 150–160 (2016).

[12] Z. Kang, K. A. James, Multimaterial topology design for optimal elastic and thermal response with material-specific temperature constraints, International Journal for Numerical Methods in Engineering 117 (10) (2019) 1019–1037 (2019).

[13] X. Zhu, C. Zhao, X. Wang, Y. Zhou, P. Hu, Z.-D. Ma, Temperature-constrained topology optimization of thermo-mechanical coupled problems, Engineering Optimization (2019) 1–23 (2019).

[14] X. Zhao, M. Zhou, O. Sigmund, C. S. Andreasen, A "poor man's approach" to topology optimization of cooling channels based on a darcy flow model, International Journal of Heat and Mass Transfer 116 (2018) 1108–1123 (2018).

[15] S. Kambampati, H. A. Kim, Level set topology optimization of cooling channels using the darcy flow model, Structural and Multidisciplinary Optimization (2020) 1–17 (2020).

[16] J. Alexandersen, C. S. Andreasen, A review of topology optimisation for fluid-based problems, Fluids 5 (1) (2020) 29 (2020).

[17] J. A. Sethian, A. Vladimirsky, Fast methods for the eikonal and related hamilton–jacobi equations on unstructured meshes, Proceedings of the National Academy of Sciences 97 (11) (2000) 5699–5703 (2000).

[18] J. A. Sethian, Level set methods and fast marching methods: evolving interfaces in computational geometry, fluid mechanics, computer vision, and materials science, Vol. 3, Cambridge university press, 1999 (1999).

[19] P. D. Dunning, H. Alicia Kim, A new hole insertion method for level set based structural topology optimization, International Journal for Numerical Methods in Engineering 93 (1) (2013) 118–134 (2013).

[20] S. Kambampati, H. Chung, H. A. Kim, A discrete adjoint based level set topology optimization method for stress constraints, Computer Methods in Applied Mechanics and Engineering 377 (2021) 113563 (2021).

[21] P. D. Dunning, H. A. Kim, G. Mullineux, Investigation and improvement of sensitivity computation using the area-fraction weighted fixed grid fem and structural optimization, Finite Elements in Analysis and Design 47 (8) (2011) 933–941 (2011).

[22] J. Chin, S. L. Schnulo, T. Miller, K. Prokopius, J. S. Gray, Battery performance modeling on sceptor x-57 subject to thermal and transient considerations, in: AIAA Scitech 2019 Forum, 2019, p. 0784 (2019).

[23] J. A. Cicero, F. L. Feiter, J. Mohammadi, Statistical loads data for cessna 172 aircraft using the aircraft cumulative fatigue system (acfs), Tech. rep., SYSTEMS AND ELECTRONICS INC ELK GROVE VILLAGE IL (2001).

[24] L. Martín-Martín, J. Gastelurrutia, N. Nieto, J. C. Ramos, A. Rivas, I. Gil, Modeling based on design of thermal management systems for vertical elevation applications powered by lithium-ion batteries, Applied Thermal Engineering 102 (2016) 1081–1094 (2016).

[25] G. Allaire, F. Jouve, A.-M. Toader, Structural optimization using sensitivity analysis and a level-set method, Journal of computational physics 194 (1) (2004) 363–393 (2004).